Emission Characteristics of Passively Fed Electrospray Microthrusters with Propellant Reservoirs

Emission characteristics of passively fed electrospray microthrusters with propellant reservoirs

David Krejci* and Fernando Mier-Hicks†
Massachusetts Institute of Technology, Cambridge, MA, 02139, USA
Robert Thomas‡ and Thomas Haag§
NASA Glenn Research Center, Cleveland, OH, 44135, USA
Paulo Lozano¶
Massachusetts Institute of Technology, Cambridge, MA, 02139, USA

We present the characterization of a miniaturized ionic liquid electrospray thruster for Nanosatellite applications. The thruster investigated features an emitter array of 480 emitter tips per square centimeter and a 1 cubic centimeter propellant tank with an entirely passive propellant supply, and is operated at a power level of < 0.15W. The paper presents energy-, and mass-resolving beam spectroscopy of the packaged thruster system, as well as two independent thrust measurements. This allows to derive thruster performance parameters under realistic firing conditions, including individual thruster efficiency contributions, specific impulse and thrust. Total thruster efficiencies of 36%, specific impulse of ~ 760s, including all losses, and thrust of $11 - 12.5\mu$N are presented, at emission currents of 150μA, for a device of ~ 1cm^2. Current emission data without current decay of ~ 90h is presented, with a maximum of 172h.

Nomenclature

f_i	Ion current fraction, -
$f(\Phi)$	Current distribution function, -
g_0	Standard acceleration due to gravity, m/s^2
I	Current, A
I_{em}	Emitted current, A
I_{sp}	Specific impulse, s
I_{sp}^{ideal}	Loss-free specific impulse, s
L	Drift length, m
q/m	Charge-to-mass ratio, C/g
t	Time, s
T	Thrust, N
V_B	Effective beam acceleration potential, V
V_e	Emitter potential, V
V_{ex}	Extractor potential, V
F	Force, N
m	Mass, kg
$\dot{m}$	Mass flow, kg/s

*Research Scientist, Department of Aeronautics and Astronautics, 77 Massachusetts Avenue, krejci@mit.edu, AIAA Member.
†Ph.D. Candidate, Department of Aeronautics and Astronautics, 77 Massachusetts Avenue.
‡Research Engineer, In-Space Propulsion Systems, 21000 Brookpark Rd., AIAA Member.
§Aerospace Engineer, In-Space Propulsion Systems, 21000 Brookpark Rd., AIAA Member
¶Professor, Department of Aeronautics and Astronautics, 77 Massachusetts Avenue, AIAA Member

η Efficiency, -
Φ Beam opening half angle, °
Subscript
E Energy
i Ionization
P Polydispersive
RPA Retarding potential analyzer
ToF Time-of-Flight
tr Transmission
Φ Angular

I. Introduction and electrospray principle

High efficiency propulsion is considered as an enabling technology in the growing field of Nanosatellites, with advanced scientific and commercial missions, allowing formation flight, orbit change maneuvers and active deorbiting, amongst others [1]. The thruster presented in this work is a miniaturized, efficient electrostatic electrospray thruster, based on microelectromechanical systems (MEMS) fabrication processes, complying with stringent volume, mass and power requirements imposed by Nanosatellites.

Electrospray thrusters are a class of electric thrusters that produce thrust by acceleration of ions or droplets after extraction from an electrically conductive liquid surface under an applied electrostatic field. To minimize thruster potentials necessary to achieve the local field strength necessary for charged particle extraction from the liquid bulk, the propellant is typically applied onto a field enhancing structure, such as a needle or sharp emitter tip, in conjunction with a high-voltage extraction grid, as shown in Figure 1. In the process of ion, or droplet, extraction by electric fields, the liquid deforms into a sharp, cone-shaped meniscus, equilibrating electrical pull and surface tension and upstream pressure. The increased electric field strength at the cone tip leads to the extraction of charged particles, which are then accelerated to produce thrust [2]. Typically two regimes of operation, or a mixture of these, occur: the cone-jet regime, in which the meniscus breaks up into droplets [3] and the ionic regime with pure ion extraction and accordingly higher specific impulse [4, 5]. The ionic mode is obtained utilizing ionic liquids as propellant, which are room temperature molten salts consisting of chemically stable mixtures of positive and negative charges. Spacecraft charging is avoided by firing in module pairs, with opposite charge and alternating the polarity periodically to maintain chemical balance and prevent electrochemical decay [6]. Due to the negligible vapor pressure of the ionic liquids [7] there is no need for propellant pressurization. These electrospray thrusters therefore allow for passive feed systems, rendering hard-to-miniaturize components such as valves unnecessary and lend themselves well towards miniaturization [4]. Electric thrusters generally feature high specific impulse values compared to chemical thrusters, since propellant exit velocities are not limited to chemically storable energy. However, miniaturized electric thrusters usually feature low thrust levels. To increase thrust, arrays of emitters have been proposed and successfully tested [8, 9, 10, 11, 12, 13, 14, 15]. The possibility of ion emission, as opposed to droplet emission, for the ionic liquid EMI-BF_4 was experimentally shown using spectrometric characterization measurements[16, 17, 18].

In this work, we present the characterization of the emission from porous emitter arrays featuring 480 emitter tips for fully packaged, highly miniaturized thrusters. Studies on performance characterization focusing on measurements taken directly after wetting of the emitter substrates are available [12, 19], including characterization of devices on different thrust stands [15]. This study is dedicated to characterizing emission under realistic firing conditions of a thruster including a fully sized propellant reservoir to ensure steady state propellant distribution and sustaining emission over extended time periods. We present spatially and energy-resolving beam measurements and time-of-flight analyses of the emitted particle beam. In addition, we present independent direct thrust measurements. This allows us to draw conclusions on the state of the emission, characterize thruster performance parameters such as thrust efficiency and specific impulse and provide a baseline of a complete propulsion system that could help guide future developments.

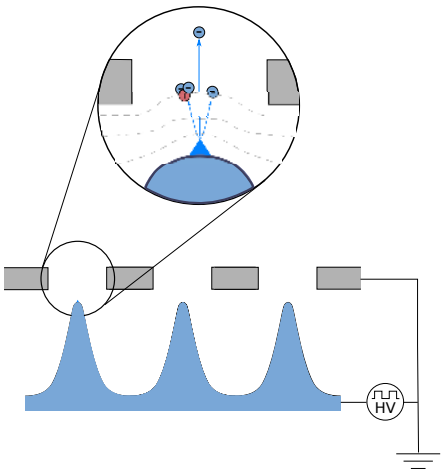

Figure 1. Electrospray principle with charged particle extraction from menisci on top of porous emitter structures

II. Description of the microthruster

The microthrusters investigated in this study consist of an array of 480 emitter tips, manufactured by laser ablation out of a single piece of porous glass with approximate footprint of $1x1$cm, arranged in a triangular pattern [20, 21] with an average emitter tip height of 175μm. The emitter tips have an apex radii of approximately 15μm and pore sizes are typically found between 1 and 10 μm. An optical image of the emitter tip structures is shown in Figure 2(a). This emitter chip is bonded to a silicon frame used for packaging and alignment of the emitter structures. This square silicon packaging frame features four corner posts with an insulating Pyrex layer to electrically insulate the high potential emitter grid from the extractor grid. The latter is attached to the corner posts of the frame, allowing for alignment of the individual apertures to the emitter tips. Optical investigation of the emitter tips in the array confirmed emitter tip heights of 160-175 μm. The apexes of the tips are aligned in the same plane as to lower plane of the extractor grid, whose apertures are 300 μm in diameter. Typical alignment accuracy is found to be better than 25μm. This emitter-extractor package is then bonded to a propellant tank manufactured in PEEK plastic, as shown in Figure 2(b). The tank houses a distal electrode, manufactured from pyrolized carbon aerogel [22, 23] with large internal surface area. Propellant supply flow is managed passively by capillary forces only. Loading the thruster with ionic liquid is performed in vacuum after outgassing of both the liquid and the thruster to avoid gas trapping, which could trigger discharges during thruster operation [24]. EMI-BF_4 was used as the standard propellant throughout this study, unless otherwise indicated. The thrusters investigated in this work are the building blocks of the Scalable ion Electrospray Propulsion System (S-iEPS), a Cubesat-sized propulsion unit developed under the NASA Microfluidic Electrospray Program (MEP) [25] fitting in an envelope of $<$ 200cc. An image of the fully integrated unit is shown in Figure 2(c).

III. Methods

III.A. Emission current and interception

Emission behavior in terms of emitted current as a function of applied emitter potential was determined by applying three successive voltage scans in a triangular profile over the investigated voltage range, with a period of 60s. High voltage was generated and measured using a Matsusada AP-3B1-L2 with $\pm$1V accuracy in the voltage monitor. Both emitted current, that is the current drawn by the emitter from the laboratory power supply, and the intercepted current, which is defined as the current measured from the extractor to ground, were recorded by measuring the voltage drop across a 1kΩ resistor in conjunction with an isolation amplifier (Analog Devices AD210JN), leading, after calibration with resistive load, to a measurement accuracy of $\pm 0.1\mu$A. Averaging of the recorded data was performed incorporating error propagation.

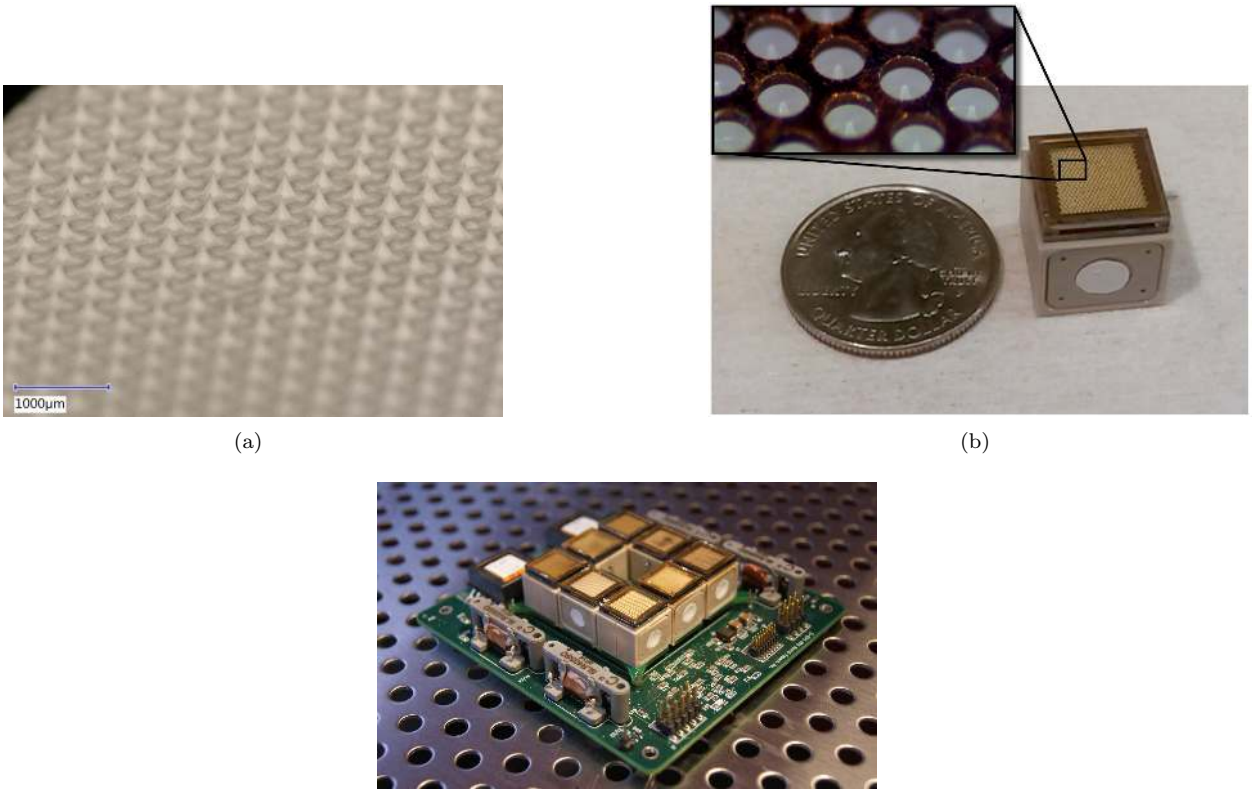

(a) (b)

(c)

Figure 2. Otical image of porous emitter array (a) and fully packaged thruster including 480 emitter array, acceleration chamber and passive propellant management system featuring 1ml tank volume (b) and fully integrated S-iEPS unit (c)

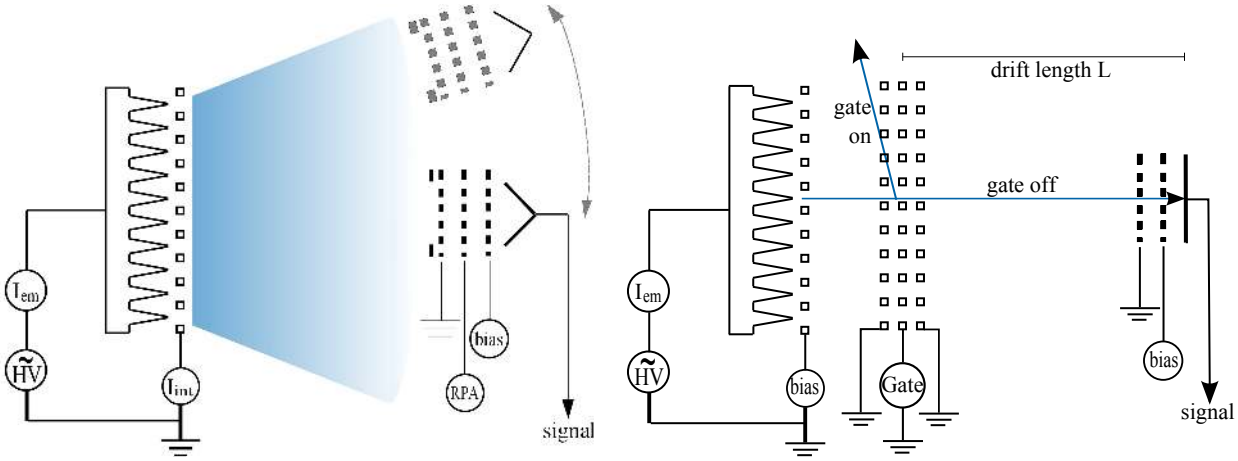

(a) RPA and spatial beam distribution measurement (b) Time-of-Flight measurement

Figure 3. Experiment configurations

III.B. Energy distribution

A retarding potential analyzer (RPA) was used to measure the energy distribution of the charged particle beam, using a singly charged species approximation for the beam. The RPA instrument consisted of a Faraday cup of $1/4''$ (6.35mm) aperture, with a grounded entrance grid, followed by the retarding potential grid and a bias grid for electron repulsion upstream of the Faraday cup. The instrument schematic is shown in Figure 3(a). The RPA detector was, if not mentioned otherwise, positioned directly at the emitter's central thrust axis at a distance of 60mm from the extractor grid. Measurements were performed by operating the emitter in single polarity, with 20 successive scans of the retarding potential from zero to the emitter potential incremented by 100V, both increasing and decreasing, with a period of 20s. Recorded data was then reduced by averaging over all scans, incorporating error propagation. Current was measured using a Keithley 6514 electrometer with femto Ampere accuracy. The largest error contribution in this experiment was found in the voltage ripple of the retarding grid of nominally $\pm$5V.

III.C. Spatial beam distribution

The spatial beam distribution was recorded using the same Faraday cup as described in Section III.B, mounted on a rotary arm 60mm from the extractor surface, able to move from $-90°$ to $+90°$ from the central thrust axis. Rotary motion was controlled by an electric motor in conjunction with a solid shaft rotary feedthrough and position switches at $\pm 90°$. The measurement principle is shown in Figure 3(a), with the RPA grid grounded. Angular position was read using an incremental angular encoder with 2500 counts per revolution. Typically 20 scans over the entire hemisphere were performed with the thruster being continuously operated in single polarity at the stated current, with data being reduced by averaging, incorporating error propagation. Current was measured using a Keithly 6514. The main source of error in this measurement was an offset present when aligning the thruster with the rotation instrument's zero axis upon thruster mounting, which was measured $< 5°$. The error introduced by approximating the finite dimensions of the emitter as a point source was estimated to be less than $< 2.5°$.

III.D. Mass distribution

Knowledge on the mass distribution of the emitted ion beam allowed the identification of relative fractions of charged ions, solvated ions, droplets, or products from fragmentation events in the beam, allowing the determination of the average charge to mass ratio of the emitted beam and thus the specific impulse. To determine the beam composition, Time-of-Flight (ToF) measurements were performed in a large vacuum chamber facility ($1.5x1.6$ m, cryopumped, pumping speed 7000 liters/sec Xenon, chamber base pressure: $< 5 \times 10^{-6}$ torr) to minimize chamber effects. Figure 3(b) shows a schematic of the ToF setup used, with a free drift length of 1.6m between the collector and the electrostatic gate. The collector consisted of a grounded grid, succeeded by a bias grid to suppress secondaries, and a detector plate of 20cm diameter, made out of copper. The sides of the entire collector structure were shielded from ambient charges. A stopping gate configuration was used to interrupt the emitted ion beam. In this configuration, the gate was switched to a potential higher than the emitter potential using a fast square waveform, therefore interrupting the beam of charged particles. The electrostatic gate consisted of a series of three highly transparent grids, with the high voltage pulse (960V) applied to the center grid, enclosed by grounded grids up- and downstream to ensure a potential free drift zone. The signal was amplified by a custom made transimpedance amplifier and recorded by an oscilloscope (Agilent Technologies DSO-X 3024A) set to 2000 trace averaging. The main uncertainty in this measurement for determining the specific impulse originated from signal noise obstructing the trailing edge of low velocity particles. A detailed discussion on an approach used to overcome this issue and resulting measurement accuracy is given in Section V.A.1.

III.E. Extended testing

During extended duration experiments, applied emitter polarity was alternated using a period of 30s to avoid charge imbalance in the propellant reservoir. Average specific impulse was determined by conducting tests with relatively long firing durations, with continuous recording of time traces of applied potential as well as emitted and intercepted currents, allowing integration of the net emitted current, with an accuracy of $\pm 0.1\mu$A. Propellant consumption was determined as the difference in weight of the packaged thruster before and after the test. Humidity intake before the test was avoided by storage in a controlled low humidity

($< 20\%$) environment before weight determination, and by determining the weight right after venting of the vacuum chamber. Applicable measurement accuracies include the current monitor accuracy ($\pm 0.1\mu$A) and the measurement uncertainty of the scale of 0.1mg.

III.F. Thrust

Two different configurations were used for independent direct thrust measurements:

III.F.1. MIT Cubesat testbed

This thrust measurement was based on a magnetically levitated satellite mockup containing a power supply and two thrusters in a rotational thrust configuration. Rotational position and movement of the levitated satellite were monitored and used, in conjunction with the knowledge of the inertia of the system, to determine the thrust exerted by the two thrusters. This setup includes an eddy current break to counteract and desaturate rotational movement, as well as a charge sensor to investigate eventual PPU ground drift. A detailed description of this measurement configuration as well as achievable accuracies can be found in Ref. [26]. The total measurement uncertainty of this instrument was calculated from individual measurement inaccuracies, including sufficient margin, as $\pm 1\mu$N. Uncertainty in high side emission current measurements are conservatively estimated at 10%, including measurement uncertainty and current drifts due to long measurement durations. Measurements were performed in a $1.5x1.6$m, cryopumped vacuum chamber (pumping speed 7000 liters/sec Xenon) with a base pressure of $< 5 \times 10^{-6}$ torr and include thrusting times of 20 minutes for each emission current setting.

III.F.2. NASA thrust balance

This setup consisted of a torsional-arm balance, with thrust being a function of a known spring constant and the arm displacement. A counterweight was placed at the opposite end of the arm from the testbed, which minimized gravitational influence on the thrust balance. The arm displacement was measured by a linear variable differential transformer (LVDT) with a resolution of $\pm$ 2 μm [27]. The measured force was calibrated in-situ and under vacuum prior to each test sequence. Three free-hanging weights, each with a mass of 3.1 mg, were strung on a fiber and passed over a pulley to align the calibration force with the axis of the testbed. Oscillation of the thrust balance arm was damped with a small solenoid magnet driven by a differential amplifier. Gain of the amplifier was normally tuned to achieve critical damping, but could be switched off as needed to allow un-damped isolation of the balance. To minimize uncertainty due to drift in the thrust signal, the thruster was turned off between throttle points to re-check the datum point. The thrust balance was operated in a cylindrical chamber of 1.5 m diameter and 4.5 m length, evacuated by four oil diffusion pumps with a background pressure of 9.7×10^{-7} torr. Multiple measurements have been performed for each current setting, with resulting measurement uncertainty of $< 6\%$ for the tests presented in section IV.C.6.

IV. Results

IV.A. Description of measurements, measurement protocols, and test matrix

Investigations of the full emitter (Section IV.C) were performed for the packaged thruster including propellant tank to ensure constant emission properties throughout extended experiment durations. In this configuration, the propellant tank was filled with ionic liquid, and the high voltage was contacted to the liquid using porous distal electrodes. Only ToF of the full array and single emitter experiments (Section IV.B) were conducted without dedicated propellant supply since total propellant consumption was small. In these tests, a small amount of propellant was stored in a piece of microfiber glass attached to the backside of the glass chip, mimicking the propellant supply of a fully packaged thruster.

Each emitter was subjected to a conditioning procedure at initial startup to ensure uniform propellant distribution. This propellant priming procedure consisted of applying an voltage about 50% larger than the expected nominal value during a period of about $10 - 20$ minutes. These values depend on the specific geometry and surface wetting condition of the thruster array.

After stable emission was achieved, defined as the absence of apparent change in emission current for constant applied emitter potential over multiple polarity switching cycles, the thruster's emission characteristic

was determined by recording the emission currents as a function of applied emitter potential, as discussed in Section III.A. Characterization experiments were performed at an emission current of $I_{em} = 150\mu$A, a value determined primarily by the NASA MEP requirement of 100μN for the full propulsion system* and the low fraction of intercepted to emitted current found for this operational point. This corresponds to an average emission current of $\sim$ 300nA per emitter tip, consistent with single emitter operation per tip. While emitters were typically operated in a single polarity during most characterization experiments described in Section III including spatial beam distribution, RPA and ToF measurements, a polarity alternation scheme with switching periods of $30s$ was typically employed during long duration operations to avoid electrochemical decay.

The propellants EMI-BF_4 and EMI-DCA were purchased from Ionic Liquids Technologies Inc., with purity of $\geq$ 97.0% and $\geq$ 98.5% respectively. EMI-$GaCl_4$ was synthesized in house, with no information available on its purity.

IV.B. Single emitter characterization

In order to interpret data recorded for the full emitter array, it is informative to know the emission characteristics of a single emitter tip of such arrays. In this study, all emitter tips of an existing emitter array were mechanically removed except one emitter located in the center of the glass chip. This way, the emission behavior of a single tip could be studied, while maintaining the same alignment and packaging features of the full thruster, thus allowing for direct comparison. Due to the significantly decreased propellant consumption when compared to the full array, no dedicated propellant tank was necessary, as discussed in Section IV.A.

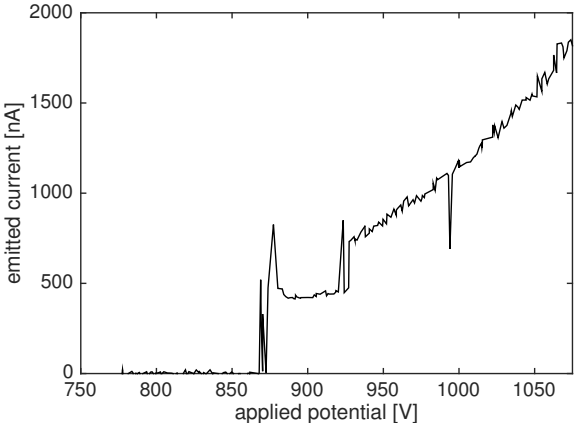

Figure 4. Emitted current as a function of applied emitter potential showing discrete steps indicating the onset of a new emission site

Figure 4 shows the current emitted from a single emitter tip as a function of applied voltage. The distinct current step associated with the onset of the main emission site, followed by a moderate increase of the current emitted by this emission site with increasing potential, is easily identifiable and was independently confirmed in Ref. [28] by spatial scanning of the emission sites. The onset current for this emission site is found to be $\sim$ 500nA. With increasing electrical stressing, the onset of a secondary emission site is clearly noticeable at $\sim$ 925V, followed again by continuous increase in current for increasing emitter potential. Angular divergence and energy-resolving measurements were first conducted at an emission current of $I_{em} = 500$nA. The emission potential was then further increased until a second step in emission current was noticed, indicating the onset and establishment of a secondary emission site. Again, angular divergence measurement and energy-resolving measurements were performed at this emission condition.

Figure 5 shows the angular beam distribution for the single emitter corresponding to the two investigated emission currents. The first key finding in this data is that the first emission site is not located centrally, which would constitute the point of highest electric field in an ideal emitter. This is most likely caused by

*NASA MEP: `http://gcd.larc.nasa.gov/wp-content/uploads/2014/01/FS-MEP_factsheet_130124.pdf`, last accessed: Oct. 19, 2015

blockage of the emitter apex or tip irregularities, given the fact that tips radii of curvatures are in the order of magnitude as the largest particle sizes found in the porous glass.

The second finding is that the increased stressing due to potential increase - up to a point where a new emission site is opened up - did not significantly change the shape and location of the main emission site.

The third important finding is that the secondary emission site is located almost exactly mirrored to the first emission position, further suggesting blockage of the emitter apex and making it inaccessible to liquid, thus making a surface around the apex being the most favorable location for emission. It should be noted that, while the angular scan is only capable of capturing the beam in a single plane, monitoring the emission current indicates that no additional emission sites were present when conducting this study. However, since the setup does not ensure that the sensor passes through equal parts of the beamlets, the recorded data does not allow conclusions regarding the relative intensity of the beamlets. This experiment was repeated in positive emission polarity with similar results.

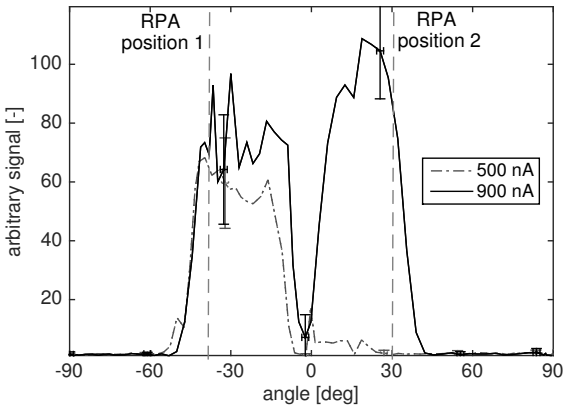

Figure 5. Angular beam divergence data for single emitter in positive emission polarity showing one and two emission sites, dashed lines indicate positions of RPA measurements.

After stopping and restarting emission repeatedly to show stability of position of the emitted beams, RPA measurements were performed at different locations ($-40°$ and $+30°$) corresponding to the two individual beams. This was done for different emission current levels, corresponding to the presence of one (I_{em} = 500nA) and two beams (I_{em} = 900nA). The resulting, normalized, RPA data are shown in Fig. 6.

The first key finding of this is that the main emission site indicates a very narrow energy distribution close to the emission potential and only little indications of particle breakup events, in which solvated ions break up into a neutral and a lighter ion at some point during or after acceleration [29, 30]. Secondly, comparison of the RPA data recorded for the main emission site at low current levels (I_{em} = 500nA) to the scan performed in the presence of the secondary emission site (I_{em} = 900nA) shows that the energy composition of the main emission site did not change significantly despite the increased electrical stressing. However, the RPA data corresponding to the secondary emission site ($+30°$) shows a largely different distribution, with energy population distributed to values significantly smaller than the emission potential.

The possible presence of emission sites with significantly altered energy properties on the same individual emitter will later explain the broad energy spread found for the full emitter array, indicating that the energy distribution broadening is not originating from stressed emission sites but from emergence of additional emission sites which are emitting under largely different conditions, and therefore lead to different energy distribution of the emitted particles.

IV.C. Full array characterization

IV.C.1. I(V) curves

Figure 7 shows the emitted and intercepted currents as a function of applied emitter potential. At an emission current of $\pm 150\mu$A, the relative interception, that is the ratio of current intercepted by the extractor electrode to total emitted current, is $4.8 - 5.5\%$.

Figure 8 compares emitted currents as a function of applied potential for different ionic liquids. For constant emitter potentials, highest emission currents are found for EMI-$GaCl_4$, followed by EMI-DCA, due

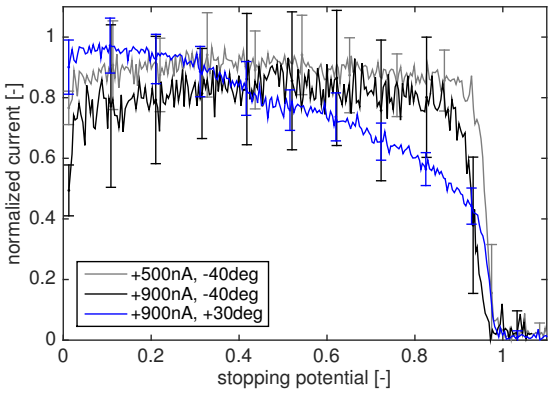

Figure 6. RPA data for single emission site, and two emission sites, taken at the indicated positions

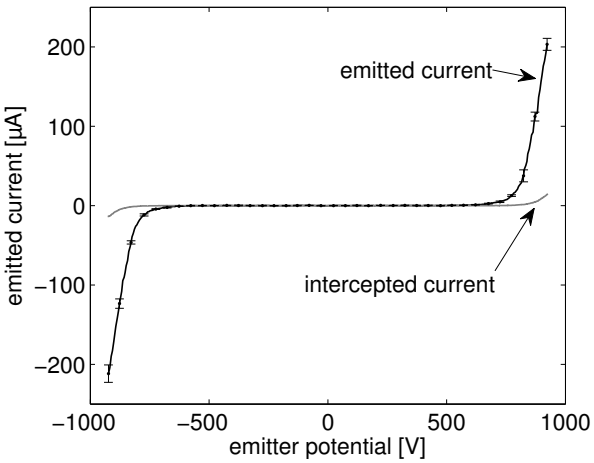

Figure 7. Emitted and intercepted current as function of applied potential for EMI-BF_4

to the difference in stressing condition and flow properties.

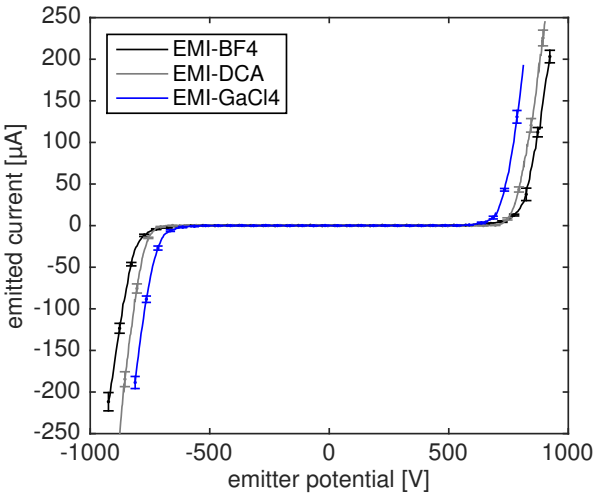

Figure 8. Emitted currents as function of applied potential for different ionic liquids

IV.C.2. RPA measurements

Figure 9 shows RPA data recored at positive and negative emission currents of $I_{em} = \pm 150\mu$A, for the three different ionic liquids. All RPA data show significant energy spreading. This is consistent with the energy-resolving results obtained for single emitters (Figure 6) which indicated the presence of emission sites with different energy properties.

Comparing the RPA data of different propellants shows increased amount of particles with lower energies, perhaps due to fragmentation, for EMI-BF_4, and, to a lesser extent for EMI-DCA, compared to EMI-$GaCl_4$.

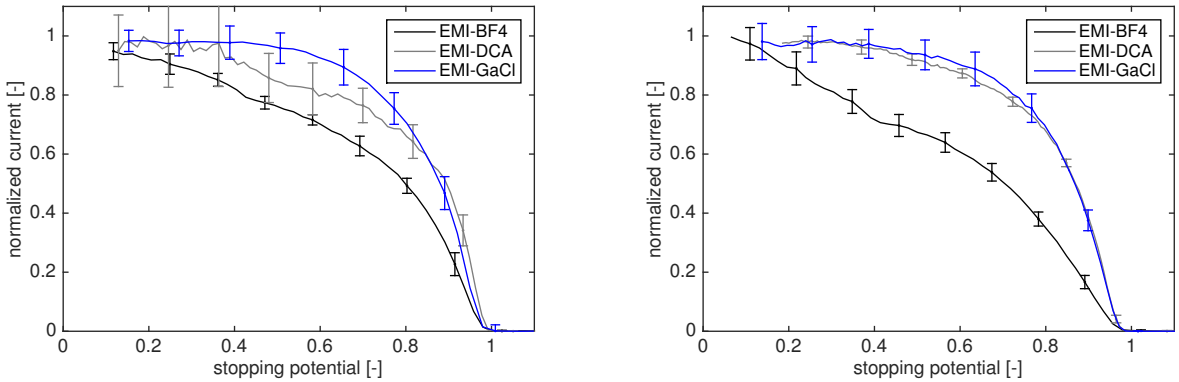

(a) positive emission mode

(b) negative emission mode

Figure 9. RPA data recorded for different ionic liquids

IV.C.3. Spatial beam distribution measurements

Figure 10 shows the beam divergence of the full emitter array measured in both polarities for different ionic liquids. Misalignment of the thrust vector, defined as the centroid of the recorded beam distribution, and the zero axis of the measurement is caused by alignment inaccuracy of the thruster with the measurement axis upon mounting.

All three measurements show good agreement of spatial emission for alternate polarities and symmetric plume shapes. A larger beam opening angle is noticed for the full beam, when compared to previously reported results for single emitters [16]. Comparison to the results presented on the spatial distribution of

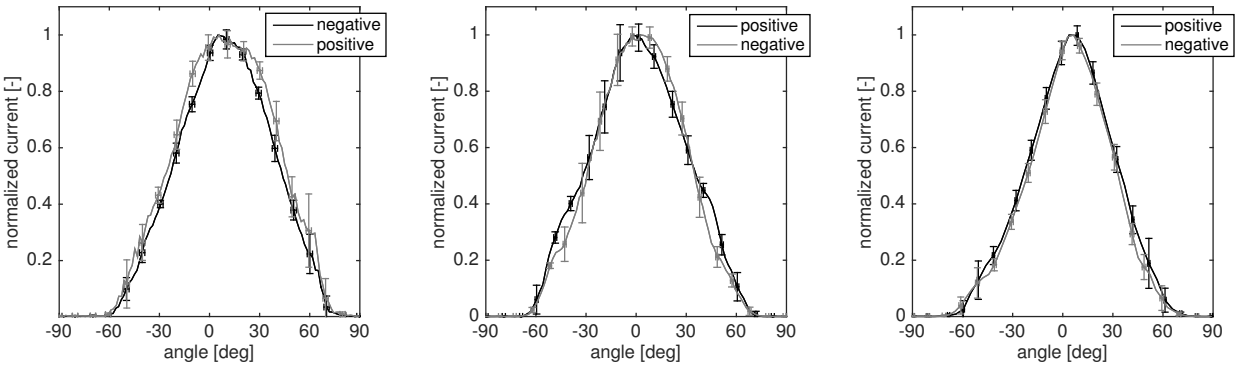

(a) EMI-BF_4 (b) EMI-DCA (c) EMI-$GaCl_4$

Figure 10. Angular beam divergence at $i = 150\mu$A for different propellants

beamlets of individual porous glass emitter tips presented in Section IV.B suggests that the increased beam spreading for the full array is caused by superposition of multiple off-axis emitted beamlets.

Comparing the spatial distributions for different propellants show that although all feature the same maximum opening angle of approximately $60 - 70°$ half angle, the full width at half maximum is smaller for EMI-DCA compared to EMI-BF_4, and decreases further for EMI-$GaCl_4$. A detailed discussion of these results is given in Section V.

IV.C.4. Time-of-Flight measurements

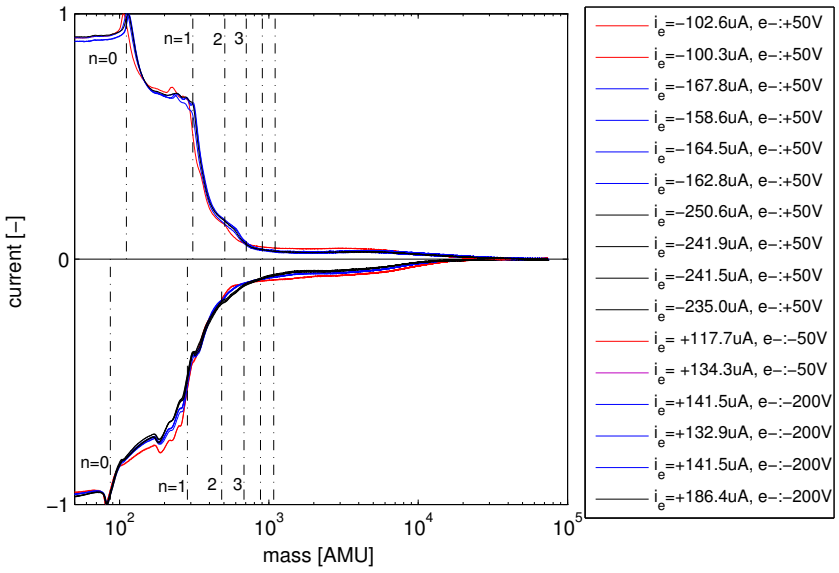

Figure 11. Time-of-Flight data for EMI-BF_4 at different emission currents

Figure 11 shows Time-of-Flight recorded for EMI-BF_4 at different emission current levels for both polarities assuming singly charged particles. The masses corresponding to the ions with solvation degree n, assuming singly charged species emitted at applied potentials (a simplification, given the width of the energy distributions), are indicated by dashed lines. Fragmentation events occurring in the beam lead to broadening of the energy distribution of the particles (Figure 9), partially obscuring the distinct current steps expected for individual beam species [31]. The recorded data clearly shows a prevailing population of monomers and dimers (single and singly solvated ions) in both polarities, with a smaller content of higher order solvated ions. In addition, a population of significantly lower specific charge, presumably charged droplets, is notice-

able in both polarities. It is interesting to notice that the composition does not vary within emission current, indicating specific impulse to be solely dependent on the square root of the emitter potential in this regime.

IV.C.5. Extended test behavior

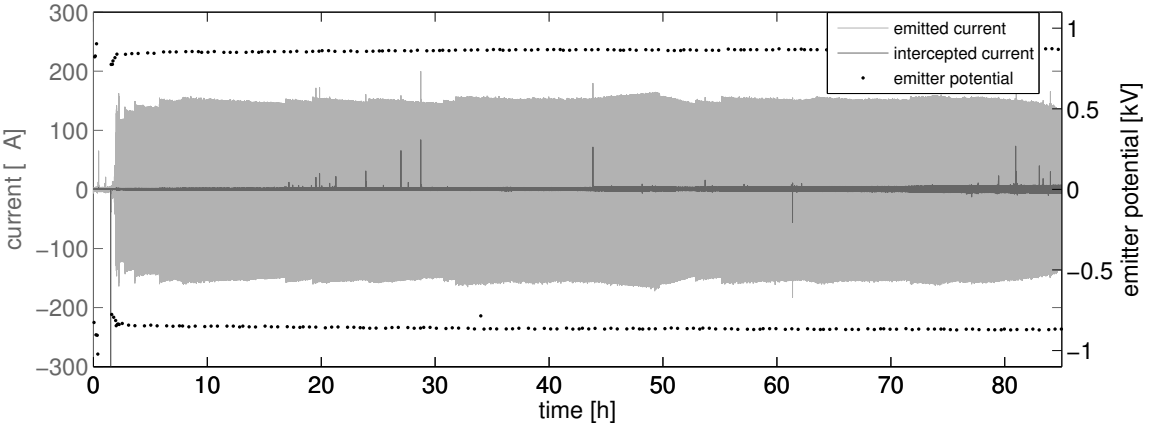

Figure 12. Emitted and intercepted current, together with applied emitter potential during a 85h test using EMI-BF_4 at average emission current of $i = 150\mu$A

Figure 12 shows the time traces of emitted and intercepted current, and applied emitter potential for a long duration test of 85h using a polarity alternation period of 30s. Occasional rapid current overshoots in emitted and intercepted signals, correlate with discharge events. In this test, the emitter potential was kept constant throughout the test, and the test duration was chosen until a noticeable decay in emitted current was observed, after approximately 85h. Current traces recorded exceeding a firing time of 85h indicate that the propellant flow may become partially interrupted, but more work is required to understand the causes of this propellant decay.

A clear trend of increasing relative interception was noticed over the duration of the entire test, ranging from $< 2\%$ to 8%. Inspection of emitters after different firing times showed formation of "bridges" of what appears to be decomposed ionic liquid linking individual emitters to the extractor, as shown in Figure 13. These bridges are anticipated to be the result of discharges, which could allow small leakage currents and contribute to an increase in the intercepted current, as their number increased over time. Over the test duration shown in Figure 12, 0.5954g of propellant were consumed. The average charge-to-mass ratio of the emitted beam was determined as $q/m = 72.5$C/g.

Ensuring constant propellant supply, the specific impulse for an ideal, loss-free thruster can be estimated as

$$I_{sp}^{ideal} = \frac{1}{g_0}\sqrt{2V_e\frac{q}{m}} \tag{1}$$

and is summarized in Table 1 for several thrusters. To exclude uncertainties in the determination of specific impulse originating from varying potentials, each of these tests was stopped as soon as a decrease in emission current was noticed unless otherwise noted. Determining the propellant mass consumed during this duration allowed us to estimate the specific impulse for constant, low emission potential, as summarized in Table 1.

For emitters $RG230$ and $RG107$, tests were conducted exceeding the onset of emission current decay (beyond $70 - 85$h into the test) caused by decreasing propellant feed flow. To maintain emission current in these tests, the emission potential was increased during these tests once current decay was observed in the measured emission current data [25] and was manually adjusted to maintain an average emission current of $I \sim 150\mu A$. It is expected that, at this stage of decreasing propellant supply and increased electrical stressing, the liquid distribution in the emitter and the emitter surface changed, effectively changing the charge to mass ratio of the emitted beam. This ultimately led to correspondingly higher average specific impulse for these tests, as indicated in Table 1. It is worth noting that, while later results from Time-of-Flight experiments indicate constant q/m for a variety of emitter potentials, these results show that change in propellant feed flow and therefore liquid distribution in the emitter can impact q/m. The longest lifetime found in a single test was 172h [25]. This test consumed 0.6306g of propellant, with an average specific charge

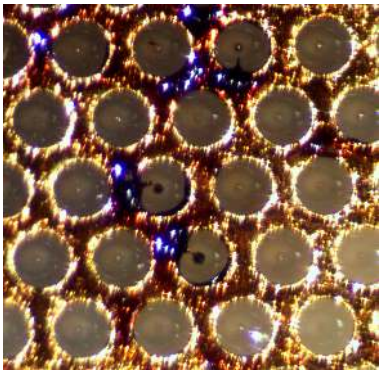

Figure 13. Decomposed ionic liquid bridging individual emitters to the extractor after long firing durations

of $q/m = 125$C/g. This leads to an overestimation of I_{sp} in the early operational phase and a corresponding underestimation for the final part of the test, given the increase in emission potential necessary to maintain the emission current level of $I_{em} = 150\mu$A.

Table 1. Longduration test data

Thruster label	q/m **[C/g]**	I_{sp}^{ideal} **[s]**	**Emitter potential [V]**	**Test duration [h]**	**Propellant consumed [g]**
RG83	76.3	1156 ± 75	~ 855	74	0.3846
RG108	72.0	1194 ± 79	~ 907	60	0.3599
RG183	72.1	1173 ± 79	~ 850	60	0.4023
RG286	72.5	1147 ± 77	~ 860	92	0.5954
Tests including manual increase of emitter potential					
RG230	82.7	1303	$\sim 870 - 1460$	126	0.6057
RG107	126.0	1717	$\sim 835 - 1480$	172	0.6306

IV.C.6. Thrust measurement

Thrust measurements were performed on individual thrusters, and pairs of thrusters, operated with EMI-BF_4 as propellant. Two independent measurements, as described in Section III, were used to measure thrust on two identical thrusters each. Thrusters were characterized firing in parallel in the magnetically-levitated balance setup at MIT, and in parallel sessions using the NASA Glenn Research Center (GRC) balance. A comparison of the recorded thrust data as a function of emitted current is shown in Figure 14.

Both measurements were able to confirm the expected linear dependency of thrust with emitted current [32] and show good correspondence with each other, within the spread of data uncertainty. A detailed discussion of the results, and cross correlation to other characterization results, can be found in Section V.

V. Discussion and Analysis

V.A. Specific Impulse

V.A.1. Indirect Estimation of Specific Impulse

The mass resolving information and the relative intensity of the different species contained in the Time-of-Flight data allow us to determine the specific impulse corresponding to the emitted particle beam, according to [2, 33]:

$$I_{sp} = \frac{T}{g_0 \dot{m}} \tag{2}$$

Where g_0 is the standard acceleration due to gravity and thrust and mass flow are calculated from

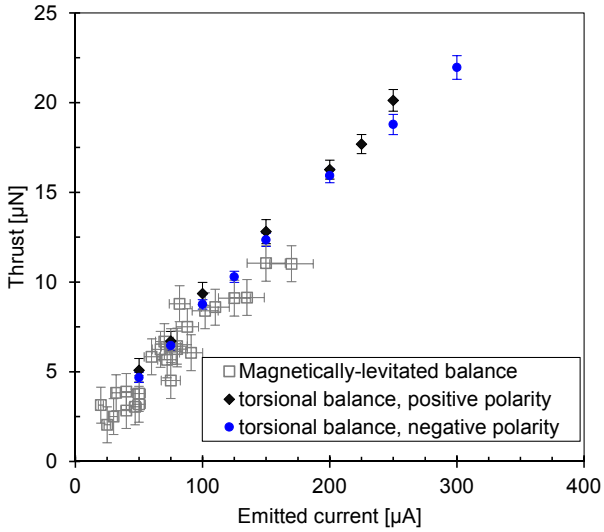

Figure 14. Thrust as a function of emission current for two independent measurements performed at NASA GRC and MIT.

Time-of-Flight data. The thrust T_{ToF} and mass flow $\dot{m}_{ToF}$ were calculated according to [15]

$$T_{ToF} = -\frac{2|V_e|}{L}\int_0^\infty t\frac{dI}{dt}dt \tag{3}$$

$$\dot{m}_{ToF} = -\frac{2V_e}{L^2}\int_0^\infty t^2\frac{dI}{dt}dt \tag{4}$$

where L is the potential free drift distance between electrostatic gate and detector, V_e the emission potential, and $\frac{dI}{dt}$ the derivation of Time-of-Flight signal current in time, normalized by surface integral.

Fragmentation upstream of the extractor electrode leads to ions with faster velocities compared to the unfragmented ion, but slower compared to non-solvated ions of the same species [31] and is therefore expected to lead to a slight overestimation of the specific impulse when derived from Eq. 3 and Eq. 4. In the experiments presented in Section IV.C.4, the extractor grid was biased to the opposite polarity of the emitter to enhance the stopping effect of the electrostatic gate. Since the gate grid is pulled to ground in the open state, the particle beam experiences a net deceleration before entering into the field free drift region between the gate and the collector. To account for this effect, the specific impulse is corrected by the square root of the ratio of applied potentials, to calculate the true specific impulse, according to:

$$I_{sp}^{true} = I_{sp}\sqrt{\frac{V_e - V_{ex}}{V_e}} \tag{5}$$

where V_e and V_{ex} are the emitter and extractor potentials respectively. As this method is highly sensible to measurement noise in the recorded data long after the measured signal decays to zero (time appears sqared within the expression for $\dot{m}$ in Eq. 4) it has been suggested to use an exponential fit in trailing edge of the droplet signal [34]. This allows to extend the integrals over the entire measurement range without introducing errors due to measurement artifacts. This approach has been used to calculate specific impulse from the data presented in Figure 11. It can then be argued that due to the importance of high mass species, the largest uncertainty is introduced by applying this exponential fit in the droplet signal's trailing edge. Uncertainty in this determination can therefore be estimated as the difference in I_{sp} data calculated using the exponential fit and the measured raw data. Figure 15 plots the calculated specific impulse based on Time-of-Flight measurements with corresponding uncertainties. In addition, the Time-of-Flight data is used to estimate the thrust. However, since effects such as the angular beam spreading are not incorporated in this analysis, significant overestimation of the thrust occurs for data based solely on Time-of-Flight measurements, compared to the direct thrust measurements in Fig. 14.

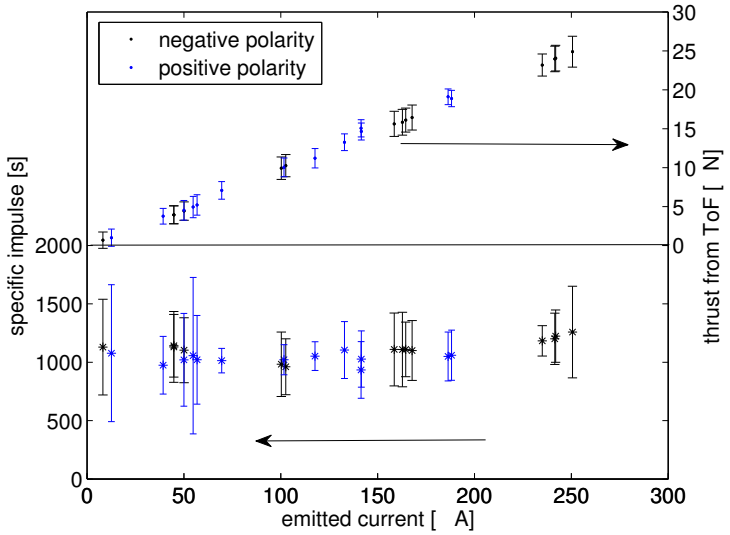

Figure 15. Specific impulse and thrust from Time-of-Flight experiments. Angular effects are not considered for thrust calculation

The derived specific impulse at emission current of $I_{em} = 150 \pm 50\mu$A is calculated as $I_{sp}^{+} = 1035.5 \pm 52$s with measurement accuracy of ± 345s for positive and $I_{sp}^{-} = 1062.1 \pm 70$s with measurement accuracy of ± 298s for negative emission polarity.

These specific impulse data can be confirmed in independent measurements, by determining the propellant mass consumption in long duration tests, in conjunction with the integrated net emitted current, as presented in Section IV.C.5. Averaging over multiple tests presented in Table 1 yields specific impulse for constant emitter potential of $I_{sp}^{ideal} = 1167 \pm 21$s with measurement accuracy of ± 79s. This is in good agreement to the specific impulse values determined via time-of-flight analysis. However, both indirectly calculated specific impulse values do not incorporate emission inefficiencies, most prominently due to angular beam spreading, as discussed hereafter.

V.A.2. Direct Calculation of Specific Impulse

Both ways of calculating the specific impulse indirectly based on Time-of-Flight and current measurements discussed in section V.A.1 do not take efficiencies that are discussed in section V.B into account. For example, the angular distribution of accelerated particles reduces the effective axial velocity of particles, which are either not captured by the Time-of-Flight detector due to geometrical constraints, or which are not accounted of when calculating the the average charge-to-mass ratio according to Eq. 1. The true specific impulse can be calculated by using thrust data presented in Section IV.C.6 and propellant mass flow determined by data provided in Section IV.C.5 according to

$$I_{sp} = \frac{T}{\dot{m} g_0} \tag{6}$$

It should be noted that thrust data and data used to determine the propellant consumption are based on separate measurements of identical thruster designs. According to the data on fire duration and total propellant consumption by mass loss in Table 1, the average propellant mass flow corresponding to an emission current of $I_{em} = 150\mu$A can be calculated as $\dot{m}_{150\mu A} = 1.69 \pm 0.19 \cdot 10^{-9}$kg/s. The corresponding thrust from Fig. 14 (GRC data) is $T = 12.6 \pm 0.7\mu$N, leading to a specific impulse of $I_{sp} = 758.9 \pm 40.7$s. Comparison to the indirectly determined specific impulse values from extended duration firings in Section V.A.1 shows that the decrease aligns well with the decrease expected from inefficiencies due to non-axial acceleration of the beam, energy inefficiencies and polydispersive efficiencies as discussed in Section V.B. However, it should be noted that the specific impulse derived using Time-of-Flight would overestimate these values, when incorporating angular and energy efficiency, by approximately 10%.

V.B. Thruster Efficiency

V.B.1. Thruster efficiency components

Table 2. Physical properties of ionic liquids at $25°C$ unless otherwise noted [35]

Ionic liquid	Density $[g/cm^3]$	Conductivity $[Si/m]$	Viscosity $[mPas]$	Surface tension $[dyn/cm]$	+/- ion mass $[amu]$
EMI-BF_4	1.28	1.28	37	45.2	111.2/86.8
EMI-DCA	1.08	2.8	21	49.05	111.2/66
EMI-$GaCl_4$	1.53	2.0	13	48.6	111.2/211.5

Emitters have been characterized using a standard procedure of scanning the applied emitter potential while recording the emitted and intercepted currents. The emission characteristics of three different ionic liquids have been studied in identical emitter configurations, showing the increased emission current of propellants EMI-DCA and EMI-$GaCl_4$ compared to EMI-BF_4. Table 2 summarizes physical parameters for these propellants. Assuming Darcy's law [36], the propellant flow rate is inversely proportional to the hydraulic impedance and thus the viscosity. For constant emitter potential, assuming similar droplet compositions, highest emission currents would be expected for the ionic liquid with smallest viscosity, EMI-$GaCl_4$, and smallest currents for EMI-BF_4, given the similar surface tensions of the liquids tested. However, additional Time-of-Flight data would be necessary to confirm this dependency. In addition to comparison of emission characteristics of different propellants, the transmission efficiency, defined as the ratio of net emitted current to the total current drawn from the emitter, was calculated using data recorded in I(V) scans. At an emission current of $I_{em} = 150\mu$A, for the propellant EMI-BF_4, the transmission efficiency, defined as the ratio of current passing the extractor without being intercepted to the total emitted current, is determined as $\eta_{tr}^{+} = 0.981 \pm 0.006$ and $\eta_{tr}^{-} = 0.982 \pm 0.011$ for positive and negative emission polarity respectively.

The spatial distribution measurements on individual emission beamlets presented in Section IV.B show half opening angles of $\sim 20°$ for both main and secondary emission sites, which is in agreement with previously reported opening angles for single emitter beams [16]. However, the spatial beam distribution results for single emitters presented in Section IV.B also indicate that individual beamlets can be emitted off-axis. Since space charge and collision effects are expected to be negligible given the charge densities involved, it could be assumed that the increased angular distribution for the full emitter array is the result of a superposition of multiple narrow, off-axis emission beamlets.

Comparison of opening angles of different propellants shows that while different liquids have different FWHM, their total spread is similar, and is most likely associated to the inability of many tips to emit on-axis.

Knowledge of the spatial beam distribution can be used to determine an angular efficiency defined as the ratio of the velocity component of the accelerated particles parallel to the main thrust axis, and the overall velocity of accelerated particles, according to [37]

$$\eta_{\Phi} = \left[\int_0^{\Phi_0} f(\Phi) cos\Phi d\Phi \right]^2 \tag{7}$$

where $f(\Phi)$ is the current distribution function over angle Φ. The axisymmetric nature of the emitted beam invoked by this expression is justified by the symmetric shape of the beam along one axis in Figs. 10. Since data was recorded over $\pm 180deg$, central thrust angle was determined as the angle at which the integrals over the distributions become equal to both sides. Eq. 7 was then used to calculate a left-handed and right-handed efficiency of the normalized data. Subsequently, an averaged efficiency was calculated incorporating error propagation calculation. Approximating the emitter as a point source, that is neglecting the finite source size, the angular efficiency for EMI-BF_4 was determined as $\eta_{\Phi}^{+} = 0.801 \pm 0.055$ and $\eta_{\Phi}^{-} = 0.828 \pm 0.045$ for positive and negative emission polarity respectively.

The combined data presented in Section IV on single emitters and full arrays allows to draw multiple conclusions on the energetic state of emission in this version of ionic liquid electrospray array thrusters. The investigation of the emission of a single emitter in Section IV.B showed the possibility of coexistence of multiple stable emission sites per emitter tip, operating in different energetic emission regimes. The data presented shows that an emission site emitting particles with a narrow energy distribution close to

the emitter potential, is not disturbed by the onset of a secondary emission site, but instead maintains its location and energetic emission properties. The energy properties of the secondary emission site were found to widely differ from the main emission site, showing an broader energy distribution with significantly lower energies, including indications of fragmentation events. This shows that emission properties likely depend on the structure of individual emission sites, and the existence of multiple emission sites per tip does not necessarily always result in a decrease in performance. Throughout testing, energetic and spatial properties of both emission sites were found repeatable. Given the proximity of the emission sites, no difference in propellant supply other than local pore size is anticipated, and the different energy spectrum is attributed to a less favorable location of the secondary emission site in terms of surface structure such as increased pore size with different liquid accumulation state on the surface. Given existing nonuniformties in propellant distribution across the emitter array due to a central, finite area propellant supply, a non-uniform distribution of emission currents across the emitter array is anticipated, facilitating regions of emitters with multiple emission sites per emitter. The emitted beam of the full thruster array is therefore considered a superposition of individual emission beamlets featuring significantly different energy properties. Such a superposition explains the large energy spread found in the energy distribution recorded for full thruster arrays in Section IV.C.

The energy resolving data allows to derive an energy efficiency, defined as the ratio of effective beam acceleration potential V_B to the applied emitter potential V_e. Attributing low voltage signals to processes occurring past emission, the effective beam acceleration potential V_B is given by the voltage corresponding to the maximum of the premier peak in the ion energy distribution function. The ion energy distribution function is calculated by taking the first derivative of the measured RPA signal as a function of voltage [37, 38, 39]:

$$\eta_E = \frac{V_B}{V_e}. \tag{8}$$

For propellant EMI-BF_4, averaging over multiple emitter arrays, the energy efficiency becomes $\eta_E^+ = 0.906 \pm 0.067$ and $\eta_E^- = 0.931 \pm 0.036$ for positive and negative emission polarity respectively.

The data recorded from the Time-of-Flight experiment in Figure 11 can be used to derive the polydispersive efficiency [40] according to

$$\eta_p = \frac{\frac{T_{ToF}^2}{2\dot{m}_{ToF}}}{V_e I_{em}} \tag{9}$$

where V_e and I_{em} refer to the applied emitter potential and the total emitted current respectively. By taking data from the Time-of-Flight experiment only in these calculations, no influence from beam spreading or energy deficiency is found in Eq. 9, hence yielding the polydispersive efficiency. The thrust T_{ToF} and mass flow $\dot{m}_{ToF}$ were calculated using Eq. 3 and Eq. 4, applying the same approximation for the trailing droplet edge as discussed in section V.A.1. The polydispersive efficiency determined by averaging over all tests presented in Fig. 11 is calculated as $\eta_p^+ = 0.5323 \pm 0.0122$ and $\eta_p^- = 0.5545 \pm 0.0260$ for positive and negative emission polarity respectively. The large efficiency losses due to the presence of droplets in the emitted beam points to the importance of reducing the emitted droplet population in future emitter designs.

The total thruster efficiency can be calculated according to[37]

$$\eta_{total} = \eta_i \eta_{tr}^2 \eta_\Phi \eta_E \eta_p \tag{10}$$

with η_i being the ionization efficiency, taken as unity since no direct evaporation of neutrals is observed in ionic liquids, η_{tr} is transmission efficiency, η_Φ the angular efficiency , η_E is the energy efficiency and η_p is the polydispersive efficiency, all discussed earlier in this Section. Including error propagation analysis, the total thruster efficiency is then approximated as $\eta_{total}^+ = 0.379 \pm 0.062$ and $\eta_{total}^- = 0.42 \pm 0.068$ for positive and negative emission polarity respectively. It is noted that the major factor impacting this efficiency is due to the polydispersive efficiency caused by the presence of droplets in the emitted ion beam.

V.B.2. Direct calculation of thruster efficiency

The total thruster efficiency can be calculated according to

$$\eta_{total} = \frac{\frac{T^2}{2\dot{m}}}{V_e I_{em}} \tag{11}$$

using the directly measured thrust (section IV.C.6) and the mass flow determined by propellant consumption (section IV.C.5), in conjunction with the directly measured applied emitter voltage V_e and emitted current I_{em}. Using the same parameters as in section V.A.2 for mass flow of $\dot{m}_{150\mu A} = 1.69 \pm 0.19 \cdot 10^{-9}$kg/s and thrust of $T = 12.6 \pm 0.7\mu$N, at an emission current of $I_{em} = 150\mu$A, the directly calculated thruster efficiency, averaged over both emission polarities, becomes $\eta_{total} = 0.361 \pm 0.081$.

V.C. Extended duration testing

Firing tests over long durations at polarity alternation intervals of 30s show stable emission current for typically $40 - 80$h before current decay is observed. This decay in current has been traced back to inadequate propellant supply from the propellant reservoir, rather than processes occurring in the emitter itself. Over the lifetime, a steadily increase in intercepted current for typically $< 2\%$ to $\sim 10\%$ of the emitted current is observed. The maximum lifetime of the porous glass MEMS emitter thruster in these experiments, fired at an average design emission current of 150μA, is found to be 172h before a short between the emitter array and the extractor terminated the test. It is found that propellant accumulation on the emitter tip and discharges induced by this accumulation had caused this short.

V.D. Thrust

Two independent thrust measurements have been conducted, employing different measurement principles. Measurements taken on the different experimental setups correspond sufficiently well with each other, with larger measurement uncertainties on the magnetically levitated balance. It should be pointed out that while the torsional thrust balance is able to resolve thrust measurements according to different polarities, the nature of the magnetically levitated thrust balance necessitated firing a pair of thrusters in opposite polarity, and thrust derived is therefore an average over polarities. In addition, deriving thrust by change of rotational motion of the levitated structure also led to thrust measurements averaging over each test duration of approximately 20 minutes. The thrust data recorded for the torsional thrust balance on the other hand shows smaller measurement uncertainties and reduced standard deviation over repeated tests, and linear behavior of thrust as a function of emission current up to high emission currents.

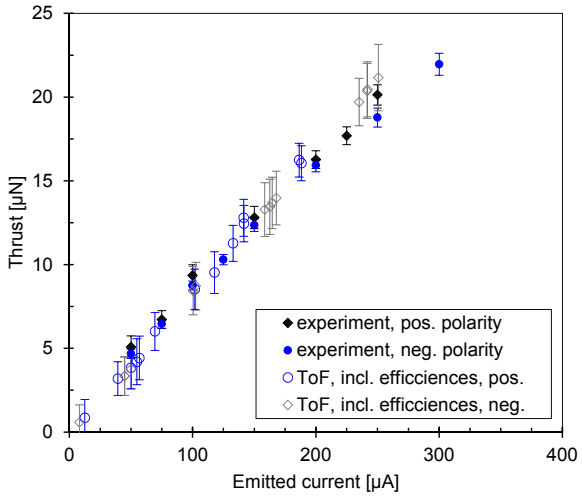

Figure 16. Comparison of direct thrust measurements (GRC balance) to thrust derived from Time-of-Flight experiments, incorporating independently derived thruster efficiency.

Direct measured thrust using the torsional thrust balance is compared in Fig. 16 to indireclty determined thrust using Time-of-Flight data by Eq. 3 , modified according to the angular and energy efficiency calculated in section V.B.1. Data from the levitational balance is omitted due in this comparison due to avoid cluttering of the plot. Interpolating values to the nominal current of 150μA, this indirectly determined thrust yields an overestimation of approximately 10%, which is within error bars.

VI. Conclusion

We present a full characterization of MEMS based ionic liquid electrospray thrusters, including two independent measurements of thrust of $T \sim 11-12.5\mu$N at emission current of $I_{em} \sim 150\mu$A for a $\sim 1\text{cm}^2$ device. Ideal specific impulse without angular beam divergence and energy losses was independently determined using Time-of-Flight measurements and extended duration testings, yielding $I_{sp}^{ideal} \sim 1050-1150$s. In addition, the specific impulse was directly calculated based on thrust measurements and propellant mass flow rate determined by extended duration firings, therefore including all thruster inefficiencies, leading to a specific impulse of $I_{sp} \sim 760$s. This decrease in actual specific impulse corresponds well to independently determined inefficiencies due to non-axial particle acceleration, energy inefficiencies and polydispersive efficiency.

We present a characterization of individual thruster efficiency contributions, including transmission efficiency, angular efficiency, energy efficiency and polydispersive efficiency. Total thruster efficiency is calculated as $\eta_{total} \sim 36\%$. A detailed discussion of individual efficiency components showed, among others, transmission efficiencies $> 98\%$, but significant losses due to angular beam spreading and the polydispersive nature of the emitted beam. While single ions and singly solvated ions are found to be the dominant species in the emitted beam, the emitters are found to operate in a mixed ion-droplet operation mode. The presence of droplets in the emitted ion beam is identified as the major cause for reduced efficiency, and highlights the importance of reduction of emitted droplets in future electrospray emitter designs.

We finally present emission behavior during extended firings, showing stable emission up to ~ 90h, before propellant feed flow decayed, necessitating increase of the applied emitter potential to sustain a nominal current level of 150μA. This characterization serves to define the fundamental operational properties of this type of propulsion systems and will be useful in guiding the design of future implementations.

Acknowledgement

This work was supported by NASA through contract No. NNL13AA12C under NASA's Game Changing Development program of the Space Technology Mission Directorate (STMD). The authors would like to thank Dr. Corey Fucetola and Alex Bost for their contributions in the fabrication of the electrospray thrusters and Catherine Miller for synthesizing the EMI-$GaCl_4$.

References

[1] Selva, D. and Krejci, D., "A survey and assessment of the capabilities of Cubesats for Earth observation," *Acta Astronautica*, Vol. 74, 2012, pp. 50 – 68.

[2] Gamero-Castano, J. and Hruby, V., "Electrospray as a Source of Nanoparticles for Efficient Colloid Thrusters," *Journal of Propulsion and Power*, Vol. 17, No. 5, 2015/04/06 2001, pp. 977–987.

[3] Carretero Benignos, J., *Numerical Simulation of a single emitter colloid thruster in pure droplet cone-jet mode*, Ph.D. thesis, Massachusetts Institute of Technology, 2005.

[4] Martinez-Sanchez, M., de la Mora, J. F., Hruby, V., Gamero-Castano, M., and Khayms, V., "Research on Colloid Thrusters," *26th International Electric Propulsion Conference*, No. IEPC 99-014, 1999.

[5] Lozano, P. and Martinez-Sanchez, M., "Experimental measurements of Colloid Thruster plumes in the ion-droplet mixed regime," *38th AIAA/ASME/SAE/ASEE Joint Propulsion Conference & Exhibit*, American Institute of Aeronautics and Astronautics, 2015/04/06 2002.

[6] Lozano, P. and Martínez-Sánchez, M., "Ionic liquid ion sources: suppression of electrochemical reactions using voltage alternation," *Journal of Colloid and Interface Science*, Vol. 280, No. 1, 2004, pp. 149 – 154.

[7] Zaitsau, D. H., Kabo, G. J., Strechan, A. A., Paulechka, Y. U., Tschersich, A., Verevkin, S. P., and Heintz, A., "Experimental Vapor Pressures of 1-Alkyl-3-methylimidazolium Bis(trifluoromethylsulfonyl)imides and a Correlation Scheme for Estimation of Vaporization Enthalpies of Ionic Liquids," *The Journal of Physical Chemistry A*, Vol. 110, No. 22, 2006, pp. 7303–7306, PMID: 16737284.

[8] Spindt, C., "Microfabricated field-emission and field-ionization sources," *Surface Science*, Vol. 266, No. 1–3, 1992, pp. 145 – 154.

[9] Pranajaya, F. and Cappelli, M., "Development of a colloid micro-thruster for flight demonstration on the Emerald nanosatellite," *37th Joint Propulsion Conference and Exhibit*, American Institute of Aeronautics and Astronautics, 2015/04/06 2001.

[10] Krpoun, R. and Shea, H. R., "Integrated out-of-plane nanoelectrospray thruster arrays for spacecraft propulsion," *Journal of Micromechanics and Microengineering*, Vol. 19, No. 4, 2009, pp. 045019.

[11] Gassend, B., *A Fully Microfabricated Two-Dimensional Electrospray Array with Applications to Space Propulsion*, Ph.D. thesis, Massachusetts Institute of Technology, 2007.

[12] Courtney, D. G., Li, H. Q., and Lozano, P., "Emission measurements from planar arrays of porous ionic liquid ion sources," *Journal of Physics D: Applied Physics*, Vol. 45, No. 48, 2012, pp. 485203.

[13] Tang, K., Lin, Y., Matson, D. W., Kim, T., and Smith, R. D., "Generation of Multiple Electrosprays Using Microfabricated Emitter Arrays for Improved Mass Spectrometric Sensitivity," *Analytical Chemistry*, Vol. 73, No. 8, 2001, pp. 1658–1663, PMID: 11338576.

[14] Arscott, S., Le Gac, S., Druon, C., Tabourier, P., and Rolando, C., "Micromachined 2D nanoelectrospray emitter [mass spectrometer applications]," *Electronics Letters*, Vol. 39, No. 24, Nov 2003, pp. 1702–1703.

[15] Courtney, D. G., Dandavino, S., and Shea, H., "Comparing Direct and Indirect Thruster Measurements from Passively Fed and Highly Ionic Electrospray Thrusters," *Journal of Propulsion and Power*, Vol. accepted for publication, 2015.

[16] Lozano, P. and Martínez-Sánchez, M., "Ionic liquid ion sources: characterization of externally wetted emitters," *Journal of Colloid and Interface Science*, Vol. 282, No. 2, 2005, pp. 415 – 421.

[17] Romero-Sanz, I., Bocanegra, R., de la Mora, J. F., and Gamero-Castaño, M., "Source of heavy molecular ions based on Taylor cones of ionic liquids operating in the pure ion evaporation regime," *Journal of Applied Physics*, Vol. 94, 2003, pp. 3599–3605.

[18] Chiu, Y.-H., Gaeta, G., Heine, T., Dressler, R., and Levandier, D., "Analysis of the Electrospray Plume from the EMI-Im Propellant Externally Wetted on a Tungsten Needle," *42nd AIAA/ASME/SAE/ASEE Joint Propulsion Conference & Exhibit*, American Institute of Aeronautics and Astronautics, 2015/04/07 2006.

[19] Legge, R. S. J., Lozano, P., and Martinez-Sanchez, M., "Fabrication and Characterization of Porous Metal Emitters for Electrospray Thrusters," *International Electric Propulsion Conference*, 2007, pp. IEPC–2007–145.

[20] Coffman, C., Perna, L., Li, H., and Lozano, P. C., "On the Manufacturing and Emission Characteristics f a Novel Borosilicate Electrospray Source," *49th AIAA/ASME/SAE/ASEE Joint Propulsion Conference*, 2013.

[21] Perna, L. E., Mier Hicks, F., Coffman, C. S., Li, H., and Lozano, P. C., "Progress Toward Demonstration of Remote, Autonomous Attitude Control of a CubeSat Using Ion Electrospray Propulsion Systems," *48th AIAA/ASME/SAE/ASEE Joint Propulsion Conference & Exhibit*, No. AIAA 2012-4289, Atlanta, Georgia, 2012.

[22] Brikner, N. and Lozano, P. C., "The role of upstream distal electrodes in mitigating electrochemical degradation of ionic liquid ion sources," *Applied Physics Letters*, Vol. 101, No. 19, 2012, pp. –.

[23] Masuyama, K. and Lozano, P., "Electrical Double Layers in Electrospray Propulsion," *International Electric Propulsion Conference*, No. IEPC-2015-178, 2015.

[24] Brikner, N., *On the identification and mitigation of life-limiting mechanisms of ionic liquid ion sources envisaged for propulsion of microspacecraft*, Ph.D. thesis, Massachusetts Institute of Technology. Department of Aeronautics and Astronautics., 2015.

[25] Krejci, D., Mier Hicks, F., Fucetola, C., Lozano, P., Hsu Schouten, A., and Martel, F., "Design and Characterization of a Scalable ion Electrospray Propulsion System," *34th International Electric Propulsion Conference*, No. IEPC-20150149, Hyogo-Kobe, Japan, 2015.

[26] Mier-Hicks, F. and Lozano, P. C., "Thrust Measurements of Ion Electrospray Thrusters using a CubeSat Compatible MAgnetically Levitated Thrust Balance," *34th International Electric Propulsion Conference*, 2015.

[27] Haag, T. W., "Thrust stand for pulsed plasma thrusters," *Review of Scientific Instruments*, Vol. 68, No. 5, May 1997, pp. 2060–2067.

[28] Guerra-Garcia, C., Krejci, D., and Lozano, P., "Spatial uniformity of the current emitted by an array of passively fed electrospray porous emitters," *Journal of Physics D: Applied Physics*, Vol. 49, No. 11, 2016, pp. 115503.

[29] Perez-Martinez, C. S. and Lozano, P. C.

[30] Miller, C. and Lozano, P., "The Effects of Metastable Solvated Ions on Electrospray Ion Thruster Efficiency," *34th International Electric Propulsion Conference*, 2015.

[31] Courtney, D. and Shea, H., "Fragmentation in Time-of-Flight Spectrometry-Based Calculations of Ionic Electrospray Thruster Performance," *Journal of Propulsion and Power*, Vol. 31, No. 5, 2015, pp. 1500–1504.

[32] Legge, R. S. J. and Lozano, P. C., "Electrospray Prpulsion Based on Emitters Microfabricated in Porous Metals," *Journal of Propulsion and Power*, Vol. 27, No. 2, 2011, pp. 485–495.

[33] Romero-Sanz, I., de Carcer, I., and de la Mora, J. F., "Ionic Propulsion Based on Heated Taylor Cones of Ionic Liquids," *Journal of Propulsion and Power*, Vol. 21, No. 2, 2005, pp. 239–242.

[34] Alonso-Matilla, R., Fernández-García, J., Congdon, H., and de la Mora, J. F., "Search for liquids electrospraying the smallest possible nanodrops in vacuo," *Journal of Applied Physics*, Vol. 116, No. 22, 2014, pp. 224504.

[35] Zhang, S., Sun, N., He, X., Lu, X., and Zhang, X., "Physical Properties of Ionic Liquids: Database and Evaluation," *J. Phys. Chem. Ref. Data.*, Vol. 35, No. 4, 2006.

[36] Whitaker, S., "Flow in porous media I: A theoretical derivation of Darcy's law," Vol. 1, No. 1, 1986, pp. 3–25.

[37] Lozano, P. and Martinez-Sanchez, M., "Efficiency Estimation of EMI-BF4 Ionic Liquid Electrospray Thrusters," *41st AIAA/ASME/SAE/ASEE Joint Propulsion Conference and Exhibit*, No. AIAA-2005-4388, Tucson, AZ, July 2005.

[38] Chiu, Y.-H., Austin, B. L., Dressler, R. A., Levandier, D., Murray, P. T., Lozano, P., and Sanchez, M. M., "Mass Spectrometric Analysis of Colloid Thruster Ion Emission from Selected Propellants," *Journal of Propulsion and Power*, Vol. 21, No. 3, 2016/11/02 2005, pp. 416–423.

[39] Fedkiw, T., *Characterization of an Iodine-Based Ionic Liquid Ion Source and Studies on Ion Fragmentation*, Master's thesis, Massachusetts Institute of Technology. Department of Aeronautics and Astronautics., 2010.

[40] Lozano, P. C., *Studies on the Ion-Droplet Mixed Regime in Colloid Thrusters*, Ph.D. thesis, Department of Aeronautics and Astronautics, Massachusetts Institute of Technology, 2003.